Letter Vol. 47, No. 6 / 15 March 2022 / Optics Letters 1549

Bound states in the continuum supported by silicon oligomer metasurfaces

Bing Meng,[1] Jianfu Wang,[1] Chaobiao Zhou,[1,3] and Lujun Huang[2,4]

[1]College of Mechanical and Electronic Engineering, Guizhou Minzu University, Guiyang 550025, China
[2]School of Engineering and Information Technology, University of New South Wales, Canberra 2602, Australia
[3]e-mail: cbzhou@gzmu.edu.cn
[4]e-mail: lujun.huang@unsw.edu.au

Received 6 January 2022; revised 10 February 2022; accepted 15 February 2022; posted 15 February 2022; published 15 March 2022

Oligomer metasurfaces have attracted a lot of attention in recent years because of their ability to drive strong resonance effects. In this work, by perturbing the symmetry of the structure, we find that there are a large number of resonance modes in the oligomer metasurfaces associated with the optical bound states in the continuum (BICs) near the communication wavelength. When the positions of two nanodisks of the hexamer oligomers are moved along the *x*- or *y*-directions at the same time, the mirror symmetry is broken, and an electric quadrupole BIC and three magnetic dipole BICs are excited. The results of near-field distribution of three-dimensional nanodisks and far-field scattering of multiple dipoles in each quasi-BIC reveal that the four BICs present different optical characteristics. It is noted that the method of symmetry breaking by moving the position of nanodisks can accurately control the asymmetric parameter of symmetry-protected BICs, which provides a route for the realization of ultrahigh quality (Q)-factor oligomer metasurfaces in experiment.

https://doi.org/10.1364/OL.453076

In recent years, dielectric oligomers regarded as the building blocks for an important type of resonant interactions at the nanoscale show great potential in electromagnetic manipulation. In 2012, Miroshnichenko *et al.* theoretically studied the Fano resonances in silicon oligomers, and their work showed the resonances were different from their plasmonic counterparts [1]. Since then, the resonance characteristics and applications of all-dielectric oligomers have been widely studied. The experimental Fano resonances in all-dielectric nanodisk oligomers were demonstrated by Chong *et al.* in 2014 [2]. Then Hopkins *et al.* studied the interaction between collective resonance and individual optically induced responses of all-dielectric quadrumers, revealing the physical mechanism of magnetic Fano resonances in dielectric quadrumers [3]. In addition to magnetic dipole and electric dipole resonances commonly found in nanoparticle oligomers, toroidal dipole [4–9] and higher-order octupole [10] resonances have also been found. It is noted that the resonant dielectric oligomers have also been widely used in various application of nanophotonics. For example, Shcherbakov *et al.* experimentally demonstrated the strong enhancement of third harmonic generation in resonant oligomers composed of three silicon nanodisks [11]. Yesilkoy *et al.* studied the imaging and biodetection in asymmetric dimer metasurfaces [12].

The quality factor (Q-factor) is an important parameter to improve the performance of oligomer nanodevices. As is well known, the regulation of dielectric oligomers holds a high degree of freedom, such as the change of size and position of each nanoparticle. Therefore, it may easily achieve an ultrahigh Q-factor by exciting some abnormal optical modes, like bound states in the continuum (BICs) that is an optical nonradiating mode [13–22]. Recently, many related works have been reported, for example, the chiral BIC metasurfaces were excited in the dimers of dielectric bars [23]; and the strong optical trapping in a quasi-BIC (QBIC) dimer system were studied by Yang *et al.* [24]. The toroidal dipole BICs in silicon nanodisk dimers were achieved by controlling the position of nanodisks [25]. In addition, the BICs of three-nanodisk [26] and four-nanodisk [27–30] oligomers have also been widely studied. Notably, compared with the BIC metasurfaces holding only one nanoparticle per unit cell [31–35], oligomer metasurfaces provide a greater possibility to excite BICs. Such metasurfaces will become an extremely important platform to obtain more flexible and stronger electromagnetic wave manipulation by exciting BICs. Moreover, when the number of nanoparticles of the oligomer is more, there will be more choices to engineer BICs.

In this work, we studied the excitation and properties of multiple BICs in silicon hexamer metasurfaces. By slightly breaking the in-plane symmetry of the structures through moving the position of nanodisks, four BICs are degenerated to QBICs. The optical near-field trapping and far-field scattering characteristics of the QBICs are discussed in detail. Our work provides a powerful approach for oligomer metasurfaces to facilitate the light trapping and manipulation at the nanoscale.

Symmetry-protected BICs, a type of BIC, can be perturbed through symmetry breaking of structures by building a radiation channel between eigenmodes and the free space, and transformed into a QBIC [32,34,36–41], whose Q-factors satisfy the following formula [32,36]:

$$Q \propto \alpha^{-2}, \tag{1}$$

where α is the asymmetry parameter. From Eq. (1), we know that the smaller the α is, the larger is the Q-factor. It is a common

method to excite symmetry-protected BICs by destroying symmetry in the geometric structure, such as split rings [38,42], asymmetric nanorods [43,44], notched cubes [34], and nanodisks [31,35,45]. Generally, to obtain a high Q-factor, the α is much smaller than 0.1 [36]. Due to the limitations of micro-nano fabrication, it is difficult to obtain small asymmetric parameters in experiment, that is, it is difficult to achieve an ultrahigh Q-factor [46]. In addition, to excite BICs by destroying the geometric structure, the introduction of symmetry breaking changes the volume of the material part in the metasurface, so the resonance wavelength of QBICs usually changes significantly when the asymmetry parameter α gradually increases. Herein, we look for a method that can accurately control the asymmetric parameters in experiment, and obtain a relatively stable resonance wavelength at the same time. Namely, by moving the relative position of the composite nanodisks. Herein, We introduce the symmetry breaking of the device by moving the position of the oligomer nanodisk to excite the BIC widely existing in the oligomer metasurface.

An oligomer metasurface composed of six silicon nanodisks is designed. The period of the unit cell P is 1500 nm, wherein the radius of each silicon nanodisk r is 180 nm and their height is 100 nm. The centers of six nanodisks are located at the vertexes of the inner hexagon of a circle with a radius of 500 nm, and we mark the nanodisks as D1–D6. The COMSOL Multiphysics and FDTD Solutions software are employed to analyze the optical properties of oligomer metasurfaces (for details, see Section 1 of Supplement 1). Figure 1(a) shows the top view of the unit cell on the x–y plane. By moving the positions of D1 and D4 simultaneously, we introduce a symmetry disturbance in the y-direction of the original structure. Herein, parameter a represents the displacement of nanodisks D1 and D4 moving together, and we specify that if moving to the right, a is positive (a>0), if moving to the left, a is negative (a<0), and a is 0 when not moving. When moving the D1 and D4 nanodisks, we find that two new modes appear in addition to the first resonance mode discussed earlier. Figure 1(b) shows the transmission spectra at different a values. We can find that when a =0, corresponding to the symmetric case, there are two radiating free BICs at wavelengths of approximately 1574.5 nm and 1589 nm which are marked as BIC-1 and BIC-2. When a changes from 0 to Â±100 nm, the symmetry of the y-axis is broken, and ideal BICs are transformed to leak modes, namely QBICs. As a increases, the

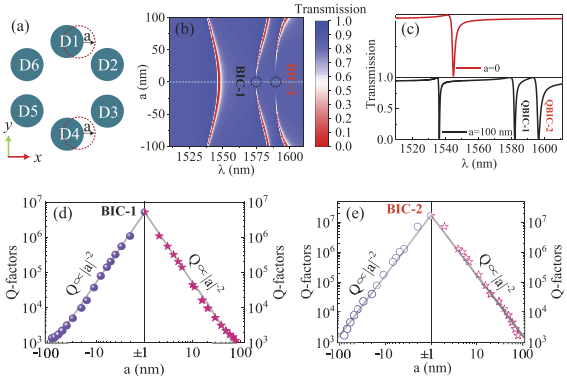

Fig. 1. (a) Top view of moved nanodisks D1 and D4, a is the distance the nanodisks move. (b) Transmission spectra as functions of wavelength and parameter a. (c) Transmission spectra for a = 0 and a = 100 nm. Q-factors of (d) QBIC-1 and (e) QBIC-2 as functions of parameter a.

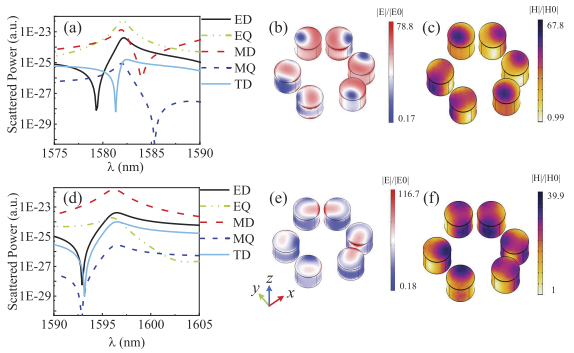

Fig. 2. Scattered power of different multipole moments for (a) QBIC-1 and (d) QBIC-2. Dashed-dotted curves, EQ; long dashed curves, MD; short dashed curves, MQ, top solid curve, ED; bottom solid curve, TD. Electric and magnetic field distributions for (b),(c) QBIC-1 and (e),(f) QBIC-2.

modes leak more, and the QBIC transmission spectra gradually widen. To see the spectral lines of the two QBICs more directly, we give transmittance spectra under the conditions of a = 0 and a = 100 nm, as shown in Fig. 1(c). For the case of a = 0, a sharp resonance is found, and its resonance characteristics are discussed in detail in Section 3 of Supplement 1. By comparison, we can obviously see the emergence of two QBICs near 1581.5 nm and 1595.5 nm which are marked as QBIC-1 and QBIC-2. The result reveals that symmetrical metasurface (a = 0) supports two symmetry-protected BICs. When the symmetry breaking of the nanodisk oligomer is introduced, the obvious asymmetric Fano resonances are produced, demonstrating the emergence of the QBIC. The Q-factors satisfy Eq. (1); here, the asymmetry parameter is defined as $\alpha = 2a/P$ and the period of unit cell P is a constant. So, the Q-factor can be finally expressed as

$$Q \propto a^{-2}, \tag{2}$$

where parameter a represents the displacement of nanodisks. It is noted that these Fano profiles of QBICs originate from the interference between discrete bound states supported by nanodisks and the free space continuum. The resonance curve can be described by the Fano formula, and the Q-factor can be also evaluated by the Fano formula (for details, see the Section 4 of Supplement 1). As shown in Figs. 1(d) and 1(e), we give the relationship between different a and Q-factors of QBIC-1 and QBIC-2. The gray lines show an inverse quadratic dependence of a, as described in Eq. (2), matching well with the variation of the calculated Q-factors.

As shown in Figs. 2(a) and 2(d), we explore the multipoles interference characteristics of the QBICs by calculating the multipoles far-field scattering power of the two modes with a fixed at 100 nm (for details, see Section 2 of Supplement 1). Figure 2(a) shows the calculation result of QBIC-1. It is shown that the electric quadrupole is the main contributor, and the magnetic dipole and electric dipole are secondary contributions, while the other dipoles are suppressed. Figure 2(d) shows the far-field scattering diagram of QBIC-2. Magnetic dipoles play a dominant role and other dipoles is strongly inhibited. The results reveal that the two QBIC modes have significant differences in multipole coupling. The results are consistent with the displacement current distributions (see Section 5 of Supplement 1).

We also study the local fields distribution within the nanodisks of both modes. Figures 2(b) and 2(c) show the distribution of

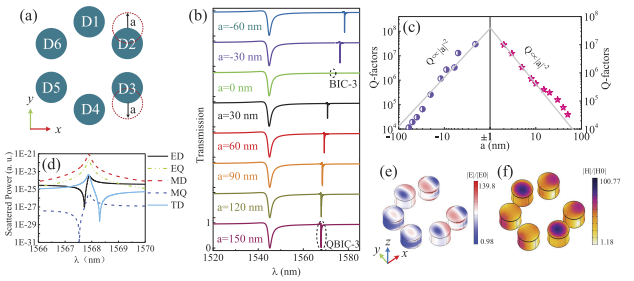

Fig. 3. (a) Top view of moved nanodisks D2 and D3. (b), (c) Transmission spectra and Q-factors of oligomer metasurfaces under different a values. (d) Far-field scattering energy of different multipole moments for QBIC-3. Dashed-dotted curves, EQ; long dashed curves, MD; short dashed curves, MQ, top solid curve, ED; bottom solid curve, TD. (e), (f) Distribution of electric and magnetic fields.

electric and magnetic fields of QBIC-1, and it can be seen that the electric fields for D1 and D2, D3 and D4 are weaker in the farther parts of the two disks, and the magnetic field is concentrated in the distant parts of the two disks. The electric fields of D5 and D6 are weaker in the nearer parts and the magnetic field is stronger in the nearer parts of the two disks. Figures 2(e) and 2(f) show the distribution of electric and magnetic fields of QBIC-2. It is found that the electric fields of D1 and D2, D3 and D4 are mainly distributed between the two disks, and there are also a small number of electric fields at the edge. The magnetic field is mainly distributed near the two disks, but weaker near the edge of the two disks. The electric fields of D5 and D6 are weak in the closer part, and the magnetic field is concentrated in the closer part of the two disks. Therefore, the local electric field distribution of the two modes is obviously different.

Next, we move the nanodisks D2 and D3 to introduce the same symmetry breaking in the y-direction. Figure 3(a) shows the top view of the changed unit cell. We set the two nanodisks away from and close to each other at the same time, and specify the displacement direction of the two nanodisks away from each other to be positive, that is, the two away from each other as $a>0$, the two closer to each other as $a<0$, and $a = 0$ without moving. As shown in Fig. 3(b), in addition to the first resonances we mentioned above, a new Fano resonance appears as $|a|$ increases, which reveals the existence of another BIC when $a = 0$ that is labeled BIC-3. The excited leakage mode is called QBIC-3. With the increase of a, the resonance spectra of QBIC-3 narrows first, disappears at $a = 0$, then appears and gradually widens. As shown in Fig. 3(c), we also calculate the Q-factor corresponding to different a to explore their dependence. It is found that the Q-factor decreases as $|a|$ increases, and the Q-factor tends to infinity at $a = 0$. When the nanodisks are close to or far away from each other, different coupling effects will occur between multiple nanodisks, which disturbs the field distribution of the resonance mode and the intensity of the local field, thus affecting the Q-factor to a certain extent. The Q-factor will be different in the two moving cases. It is noted that the leakage mode is generated by symmetry-protected BIC, so the Q-factor excited by the two moving modes still meets $Q \propto a^{-2}$.

Fixing $a = 150$ nm, we also explore the far-field radiation and near-field trapping characteristics of the QBIC-3. As shown in Fig. 3(d), magnetic dipole and electric quadrupole radiation dominate, while radiation from other dipoles is inhibited. In addition, the distributions of the electric and magnetic fields are also shown in Figs. 3(e) and 3(f). It is clear that the electric fields of D1 and D4 are mainly concentrated on the farther side pointed to by the x-axis arrow, and the magnetic fields are all concentrated inside the nanodisks. The electric fields of D2 and D3 are concentrated on the nearer parts along the x-axis, and the magnetic fields are concentrated on the farther parts. The local field trapping of nanodisks D5 and D6 is relatively weak. The results reveal that BIC-3 differs from BIC-1 and BIC-2.

Finally, we discuss the BICs for the case of symmetry breaking in the x- and y-directions. The nanodisks D3 and D5 are moved simultaneously. Figure 4(a) shows the schematic diagram of nanodisks' movement. D3 and D5 move to the left or right at the same time, and the distance to the left is specified to be positive, that is, $a>0$. If they move to the right, $a<0$, and $a = 0$ if they do not move. The mirror symmetry along the x- and y-directions is destroyed at the same time for the case of $|a|>0$. Figure 4(b) shows the transmission spectra when the a value is changed. For $a = 0$, a new BIC appears near 1575 nm, labeled BIC-4. When $|a|>0$, the symmetry of the structure is disturbed and BIC-4 is converted to radiation QBIC-4. Figure 4(c) shows the Q-factor of QBIC-4 under different a values. When $|a|=1$ nm, the Q-factor exceeds 10^7, which still satisfies the following relationship $Q \propto a^{-2}$. Figure 4(d) shows the transmission spectrum and multipole scattering spectrum lines when $a = 100$ nm. The magnetic dipole plays a major role, the electric quadrupole plays a minor role, and the contributions of other dipoles are strongly inhibited. In Figs. 4(e) and 4(f), the distribution of electric and magnetic fields at the resonant wavelength is shown. It can be seen that the electric fields of D1 and D4 are mainly distributed at the edge of the disk in the negative direction of the x-axis, and the magnetic field is localized at the center of the disk. The electric fields of D2 and D3 are localized in the middle of the disk, and the magnetic fields are distributed in the left and right edges of the disk. The main electric field and magnetic field of D5 and D6 are distributed on the edge of the disk. The electric field is in the positive direction of the x-axis, and the magnetic field is in the negative direction of the x-axis. The multipole radiation contributions of QBIC-3 and QBIC-4 are similar, their difference also can be understood through the displacement current distribution (see Section 5 of Supplement 1).

The symmetry breaking of the nanostructure is introduced by moving the position of the nanodisks. In general, in the fabrication process, the specific position parameters of nanodisks

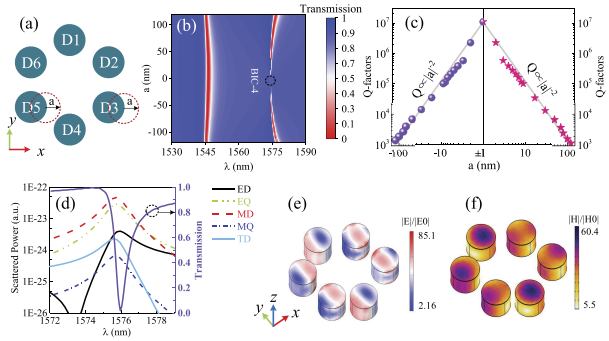

Fig. 4. (a) Schematic of moving nanodisks D3 and D5, where a is the distance the disks move. (b) Transmission spectra corresponding to the change of a from −120 nm to 120 nm. (c) Q-factor of QBIC-4 changing with parameter a. (d) Transmission spectrum and scattered radiation contributions of different multipole moments at $a = 100$ nm. Key same as in Fig. 3. (e), (f) Electric and magnetic field distribution of nanodisks at resonance wavelength when a is 100 nm.

are fixed, and then their lithographic patterns are drawn by L-Edit software. Finally, the sample is fabricated by electron beam lithography and inductively coupled plasma techniques. The fabrication process only changes the uniformity and roughness of the nanodevice, the position of the nanodisk does not move. So, the asymmetry parameter could be accurately controlled in experiment. Meanwhile, with this method to excite the BICs, the volume of the material part in the metasurface does not change, so the resonance wavelength shows minor change which is usually caused by the difference of the coupling between the nanodisks. Generally speaking, the resonant wavelength of QBICs excited in this way is relatively stable. In addition, this also has a large fabrication tolerance, and a detailed discussion can be found in Sections 6–9 of Supplement 1.

In summary, we investigate the abundant BICs in oligomer metasurfaces. By slightly breaking the inplane symmetry of the structures through moving the position of nanodisks, the multiple BICs can be transformed into QBICs. The multipole decomposition is carried out and the far field contribution and near field analysis are performed to reveal the difference of these BICs. In this way, the asymmetric parameter of symmetry-protected BICs can be accurately controlled in experiment, and the resonant wavelength of the excited QBICs is relatively stable. In addition, this method also has a large fabrication tolerance. This result provides a route for the realization of an ultrahigh Q-factor oligomer metasurface, which provides great potential for application in various micro-nano devices such as nonlinear devices, lasers, and sensors.

Funding. National Natural Science Foundation of China (12004084, 12164008); Natural Science Foundation of Guizhou Province (ZK[2021]030); Natural Science Foundation of Guizhou Minzu University (GZMU[2019]YB30, GZMUZK[2021]YB06); Construction Project of Characteristic Key Laboratory in Guizhou Colleges and Universities (Y[2021]003); Undergraduate Innovation and Entrepreneurship Training Program of Guizhou Province (202110672110).

Disclosures. The authors declare no conflicts of interest.
Data availability. Data underlying the results presented in this paper are not publicly available at this time but may be obtained from the authors upon reasonable request.
Supplemental document. See Supplement 1 for supporting content.

REFERENCES

1. A. E. Miroshnichenko and Y. S. Kivshar, Nano Lett. **12**, 6459 (2012).
2. K. E. Chong, B. Hopkins, I. Staude, A. E. Miroshnichenko, J. Dominguez, M. Decker, D. N. Neshev, I. Brener, and Y. S. Kivshar, Small **10**, 1985 (2014).
3. B. Hopkins, D. S. Filonov, A. E. Miroshnichenko, F. Monticone, A. Alu, and Y. S. Kivshar, ACS Photonics **2**, 724 (2015).
4. A. A. Basharin, M. Kafesaki, E. N. Economou, C. M. Soukoulis, V. A. Fedotov, V. Savinov, and N. I. Zheludev, Phys. Rev. X **5**, 011036 (2015).
5. G. Zhang, C. Lan, R. Gao, Y. Wen, and J. Zhou, Adv. Theory Simul. **2**, 1900123 (2019).
6. S. Xu, A. Sayanskiy, A. S. Kupriianov, V. R. Tuz, P. Kapitanova, H.-B. Sun, W. Han, and Y. S. Kivshar, Adv. Opt. Mater. **7**, 1801166 (2019).
7. Z.-J. Yang, Y.-H. Deng, Y. Yu, and J. He, Nanoscale **12**, 10639 (2020).
8. V. R. Tuz, V. Dmitriev, and A. B. Evlyukhin, ACS Appl. Nano Mater. **3**, 11315 (2020).
9. V. Dmitriev, A. S. Kupriianov, S. D. S. Santos, and V. R. Tuz, J. Phys. D: Appl. Phys. **54**, 115107 (2021).
10. P. D. Terekhov, A. B. Evlyukhin, D. Redka, V. S. Volkov, A. S. Shalin, and A. Karabchevsky, Laser Photonics Rev. **14**, 1900331 (2020).
11. M. R. Shcherbakov, A. S. Shorokhov, D. N. Neshev, B. Hopkins, I. Staude, E. V. Melik-Gaykazyan, A. A. Ezhov, A. E. M. Miroshnichenko, I. Brener, A. A. Fedyanin, and Y. S. Kivshar, ACS Photonics **2**, 578 (2015).
12. F. Yesilkoy, E. R. Arvelo, Y. Jahani, M. Liu, A. Tittl, V. Cevher, Y. Kivshar, and H. Altug, Nat. Photonics **13**, 390 (2019).
13. C. W. Hsu, B. Zhen, A. D. Stone, J. D. Joannopoulos, and M. Soljačić, Nat. Rev. Mater. **1**, 16048 (2016).
14. K. Koshelev, G. Favraud, A. Bogdanov, Y. Kivshar, and A. Fratalocchi, Nanophotonics **8**, 725 (2019).
15. L. Huang, L. Xu, M. Rahmani, D. Neshev, and A. E. Miroshnichenko, Adv. Photonics **3**, 016004 (2021).
16. Z. Sadrieva, K. Frizyuk, M. Petrov, Y. Kivshar, and A. Bogdanov, Phys. Rev. B **100**, 115303 (2019).
17. J. Tian, Q. Li, P. A. Belov, R. K. Sinha, W. Qian, and M. Qiu, ACS Photonics **7**, 1436 (2020).
18. J. Li, J. Li, C. Zheng, Z. Yue, S. Wang, M. Li, H. Zhao, Y. Zhang, and J. Yao, Carbon **182**, 506 (2021).
19. D. R. Abujetas and J. A. Sánchez-Gil, Nanomaterials **11**, 998 (2021).
20. D. R. Abujetas, Á. Barreda, F. Moreno, A. Litman, J.-M. Geffrin, and J. A. Sánchez-Gil, Laser Photonics Rev. **15**, 2000263 (2021).
21. I. A. Al-Ani, K. As' Ham, L. Huang, A. E. Miroshnichenko, W. Lei, and H. T. Hattori, Adv. Opt. Mater. **10**, 2101120 (2021).
22. J. Algorri, F. Dell'Olio, P. Roldán-Varona, L. Rodríguez-Cobo, J. López-Higuera, J. Sánchez-Pena, V. Dmitriev, and D. Zografopoulos, Opt. Express **30**, 4615 (2022).
23. M. V. Gorkunov, A. A. Antonov, and Y. S. Kivshar, Phys. Rev. Lett. **125**, 093903 (2020).
24. S. Yang, C. Hong, Y. Jiang, and J. C. Ndukaife, ACS Photonics **8**, 1961 (2021).
25. Y. He, G. Guo, T. Feng, Y. Xu, and A. E. Miroshnichenko, Phys. Rev. B **98**, 161112 (2018).
26. A. S. Kupriianov, Y. Xu, A. Sayanskiy, V. Dmitriev, Y. S. Kivshar, and V. R. Tuz, Phys. Rev. Appl. **12**, 014024 (2019).
27. V. R. Tuz, V. V. Khardikov, and Y. S. Kivshar, ACS Photonics **5**, 1871 (2018).
28. Y. Wang, Z. Han, Y. Du, and J. Qin, Nanophotonics **10**, 1295 (2021).
29. Y. Cai, Y. Huang, K. Zhu, and H. Wu, Opt. Lett. **46**, 4049 (2021).
30. A. Sayanskiy, A. S. Kupriianov, S. Xu, P. Kapitanova, V. Dmitriev, V. V. Khardikov, and V. R. Tuz, Phys. Rev. B **99**, 085306 (2019).
31. C. Zhou, X. Qu, S. Xiao, and M. Fan, Phys. Rev. Appl. **14**, 044009 (2020).
32. S. Li, C. Zhou, T. Liu, and S. Xiao, Phys. Rev. A **100**, 063803 (2019).
33. V. R. Tuz, V. V. Khardikov, A. S. Kupriianov, K. L. Domina, S. Xu, H. Wang, and H.-B. Sun, Opt. Express **26**, 2905 (2018).
34. Z. Liu, Y. Xu, Y. Lin, J. Xiang, T. Feng, Q. Cao, J. Li, S. Lan, and J. Liu, Phys. Rev. Lett. **123**, 253901 (2019).
35. Z. Zheng, A. Komar, K. Zangeneh Kamali, J. Noble, L. Whichello, A. E. Miroshnichenko, M. Rahmani, D. N. Neshev, and L. Xu, J. Appl. Phys. **130**, 053105 (2021).
36. K. Koshelev, S. Lepeshov, M. Liu, A. Bogdanov, and Y. Kivshar, Phys. Rev. Lett. **121**, 193903 (2018).
37. N. Karl, P. P. Vabishchevich, S. Liu, M. B. Sinclair, G. A. Keeler, G. M. Peake, and I. Brener, Appl. Phys. Lett. **115**, 141103 (2019).
38. L. Cong and R. Singh, Adv. Opt. Mater. **7**, 1900383 (2019).
39. J. Algorri, F. Dell'Olio, P. Roldán-Varona, L. Rodríguez-Cobo, J. López-Higuera, J. Sánchez-Pena, and D. Zografopoulos, Opt. Express **29**, 10374 (2021).
40. D. Liu, X. Yu, F. Wu, S. Xiao, F. Itoigawa, and S. Ono, Opt. Express **29**, 24779 (2021).
41. W. Huang, S. Liu, Y. Cheng, J. Han, S. Yin, and W. Zhang, New J. Phys. **23**, 093017 (2021).
42. V. Fedotov, M. Rose, S. Prosvirnin, N. Papasimakis, and N. Zheludev, Phys. Rev. Lett. **99**, 147401 (2007).
43. F. Zhang, X. Huang, Q. Zhao, L. Chen, Y. Wang, Q. Li, X. He, C. Li, and K. Chen, Appl. Phys. Lett. **105**, 172901 (2014).
44. K. Koshelev, Y. Tang, K. Li, D.-Y. Choi, G. Li, and Y. Kivshar, ACS Photonics **6**, 1639 (2019).
45. J. Wang, J. Kühne, T. Karamanos, C. Rockstuhl, S. A. Maier, and A. Tittl, Adv. Funct. Mater. **31**, 2104652 (2021).
46. J. Kühne, J. Wang, T. Weber, L. Kühner, S. A. Maier, and A. Tittl, Nanophotonics **10**, 4305 (2021).